

BEYONDPLANCK II. CMB map-making through Gibbs sampling

E. Keihänen^{3*}, A.-S. Suur-Uski^{3,7}, K. J. Andersen¹¹, R. Aurlien¹¹, R. Banerji¹¹, M. Bersanelli^{4,9,10}, S. Bertocco⁸, M. Brilenkov¹¹, M. Carbone¹⁴, L. P. L. Colombo⁴, H. K. Eriksen¹¹, M. K. Foss¹¹, C. Franceschet^{4,10}, U. Fuskeland¹¹, S. Galeotta⁸, M. Galloway¹¹, S. Gerakakis¹⁴, E. Gjerløw¹¹, B. Hensley², D. Herman¹¹, M. Iacobellis¹⁴, M. Ieronymaki¹⁴, H. T. Ihle¹¹, J. B. Jewell¹¹, A. Karakci¹¹, R. Keskitalo¹, G. Maggio⁸, D. Maino^{4,9,10}, M. Maris⁸, A. Mennella^{4,9,10}, S. Paradiso^{4,10}, B. Partridge⁶, M. Reinecke¹³, T. L. Svalheim¹¹, D. Tavagnacco^{8,5}, H. Thommesen¹¹, M. Tomasi^{4,9}, D. J. Watts¹¹, I. K. Wehus¹¹, and A. Zacchei⁸

- ¹ Computational Cosmology Center, Lawrence Berkeley National Laboratory, Berkeley, California, U.S.A.
- ² Department of Astrophysical Sciences, Princeton University, Princeton, NJ 08544, U.S.A.
- ³ Department of Physics, Gustaf Hällströmin katu 2, University of Helsinki, Helsinki, Finland
- ⁴ Dipartimento di Fisica, Università degli Studi di Milano, Via Celoria, 16, Milano, Italy
- ⁵ Dipartimento di Fisica, Università degli Studi di Trieste, via A. Valerio 2, Trieste, Italy
- ⁶ Haverford College Astronomy Department, 370 Lancaster Avenue, Haverford, Pennsylvania, U.S.A.
- ⁷ Helsinki Institute of Physics, Gustaf Hällströmin katu 2, University of Helsinki, Helsinki, Finland
- ⁸ INAF - Osservatorio Astronomico di Trieste, Via G.B. Tiepolo 11, Trieste, Italy
- ⁹ INAF/IASF Milano, Via E. Bassini 15, Milano, Italy
- ¹⁰ INFN, Sezione di Milano, Via Celoria 16, Milano, Italy
- ¹¹ Institute of Theoretical Astrophysics, University of Oslo, Blindern, Oslo, Norway
- ¹² Jet Propulsion Laboratory, California Institute of Technology, 4800 Oak Grove Drive, Pasadena, California, U.S.A.
- ¹³ Max-Planck-Institut für Astrophysik, Karl-Schwarzschild-Str. 1, 85741 Garching, Germany
- ¹⁴ Planetek Hellas, Leoforos Kifisias 44, Marousi 151 25, Greece

November 13, 2020

ABSTRACT

We present a Gibbs sampling solution to the map-making problem for CMB measurements, building on existing destriping methodology. Gibbs sampling breaks the computationally heavy destriping problem into two separate steps; noise filtering and map binning. Considered as two separate steps, both are computationally much cheaper than solving the combined problem. This provides a huge performance benefit as compared to traditional methods, and allows us for the first time to bring the destriping baseline length to a single sample. We apply the Gibbs procedure to simulated *Planck* 30 GHz data. We find that gaps in the time-ordered data are handled efficiently by filling them with simulated noise as part of the Gibbs process. The Gibbs procedure yields a chain of map samples, from which we may compute the posterior mean as a best-estimate map. The variation in the chain provides information on the correlated residual noise, without need to construct a full noise covariance matrix. However, if only a single maximum-likelihood frequency map estimate is required, we find that traditional conjugate gradient solvers converge much faster than a Gibbs sampler in terms of total number of iterations. The conceptual advantages of the Gibbs sampling approach lies in statistically well-defined error propagation and systematic error correction, and this methodology forms the conceptual basis for the map-making algorithm employed in the BEYONDPLANCK framework, which implements the first end-to-end Bayesian analysis pipeline for CMB observations.

Key words. methods: numerical – data analysis – cosmic microwave background

1. Introduction

Removal of correlated $1/f$ noise generated by detectors is a crucial step in the data processing chain for cosmic microwave background (CMB) measurements. Noise removal is most commonly done jointly with map-making. A number of different methods have been developed for this purpose. For reviews of different methods applied to *Planck*, see Poutanen et al. (2006), Ashdown et al. (2007a,b, 2009), and references therein. For a closely related discussion of Bayesian noise estimation with time-ordered CMB data, see Wehus et al. (2012).

Conventional map-making produces as initial output pixelized sky maps of CMB temperature and polarization at a given frequency. These pixelized sky maps then serve as input for the separation of astrophysical components (e.g., Planck Collaboration IV 2020), including the CMB, and further for power spec-

trum estimation (e.g., Planck Collaboration V 2020). As input, map-making takes the calibrated time-ordered information (TOI) data stream, together with corresponding detector pointing information.

The generalized least-squares methods (GLS) aim at finding the map m that maximizes the likelihood of the data $P(d | m)$, where the likelihood depends on an assumed known noise spectrum. Another widely used approach is the destriping technique (Burigana et al. 1997; Delabrouille 1998; Maino et al. 1999, 2002; Keihänen et al. 2004, 2005; Sutton et al. 2009; Kurki-Suonio et al. 2009; Keihänen et al. 2010), where the correlated noise component is modelled as a sequence of offsets, whose amplitudes are then solved for through maximum likelihood analysis and then subtracted from the timeline.

Conventional map-making, whether GLS or destriping, is a memory-intensive data processing step, since it requires that all the detector pointing information for the data set is kept in memory simultaneously. This follows from the coupling between two

* Corresponding author: E. Keihänen; elina.keihanen@helsinki.fi

signal components with very different characteristics: the sky signal (represented by a map) is dependent on the detector’s pointing on the sky, while the noise component is correlated in the time domain but independent of where the detector is pointing.

In this work we examine the possibility of solving the map-making and noise removal problem through a Gibbs sampling technique. Gibbs sampling breaks the computationally heavy map-making problem into two separate steps: noise removal and construction of the sky signal from noise-cleaned TOI. Considered as isolated steps, both are much simpler than the combined map-making procedure. As a test case we use simulated *Planck* LFI data in the context of the BEYONDPLANCK project. For an introduction to Gibbs sampling theory, and for an overview of the BEYONDPLANCK project, we refer the reader to the first paper of this series, [BeyondPlanck Collaboration \(2020\)](#).

A great benefit of the proposed procedure is that the noise removal step can be carried out separately for each *Planck* pointing period, reducing the memory requirement tremendously, as compared to conventional map-making methods. Second, in the absence of data flagging and Galactic masking, the noise removal step reduces into a simple Fast Fourier Transform (FFT) filtering operation, in which case the computational cost of noise removal is equivalent to only two FFTs of the full TOI. Flagging, however, breaks the stationarity of the data, and we examine two alternative solutions to this problem: filling of gaps with a Gibbs technique, and exactly solving the non-stationary filtering problem. As a consequence of these two facts, we are for the first time able to reduce the length of the destriping baseline to one single TOI sample, with a significantly lower combined computational cost than traditional approaches.

As a byproduct, the Gibbs map-making process also yields an estimate of the residual noise in the output products in the form of a discrete set of samples that accounts for both white and residual correlated noise, without need to compute a noise covariance matrix. The computational cost of running a full Gibbs chain, like that described in this paper, must therefore be compared to the cost of generating a full ensemble of end-to-end simulations, or the cost of evaluating a dense noise covariance matrix, in a traditional pipeline.

The main focus of this paper is on the noise removal step. For demonstration purposes, we combine noise removal with a simple pixel-based map-making procedure. For this purpose we have written a stand-alone test code, which allows us to study the map-making step in separation, independently from the Commander code ([Eriksen et al. 2008](#)) that forms the basis for the BEYONDPLANCK processing ([BeyondPlanck Collaboration 2020](#)). The great potential of the method, however, lies in a scenario where noise removal is combined within the Gibbs framework with modeling of the sky signal and instrument effects, which is the main overall goal of the BEYONDPLANCK project.

2. Methodology

2.1. Gibbs sampling procedure

We consider a time-ordered data stream from one detector of a *Planck*-like CMB experiment, which may be modelled as

$$\mathbf{d} = \mathbf{P}\mathbf{m} + \mathbf{n}'. \quad (1)$$

Here \mathbf{P} is the pointing matrix, which encodes the scanning strategy and the detector’s response to temperature and polarization, and \mathbf{m} is the pixelized sky map, which includes temperature and

polarization components in the form of I, Q, U Stokes components. Formally, \mathbf{P} is a large matrix of size $(N_t, 3N_p)$, where N_t is the number of samples in the time-ordered data stream, and N_p is the number of pixels in the sky map. In the place of $\mathbf{P}\mathbf{m}$ we could have other sky models, for instance a harmonic representation of the sky, or a parametrized foreground model. In this work we do not pursue these possibilities further, but assume the simple pixelized sky model.

The instrument noise of *Planck* LFI radiometers is well approximated as Gaussian distributed ([Bersanelli et al. 2010](#)). The noise stream can be divided into two components: correlated $1/f$ noise, and uncorrelated white noise. In the spirit of destriping, we model the correlated noise component as a sequence of constant offsets, or “baselines” of fixed length N_a . We write the noise term as

$$\mathbf{n}' = \mathbf{F}\mathbf{a} + \mathbf{n}, \quad (2)$$

where \mathbf{a} represents the baseline amplitudes, and \mathbf{F} is a matrix which formally projects them into a full data stream. With a baseline length of N_a , each column of \mathbf{F} has the value 1 along N_a adjacent elements, and the value 0 elsewhere. In the extreme limit in which the baseline length equals one sample, \mathbf{F} becomes a unity matrix and can be dropped from the equations. The last term, \mathbf{n} , represents white noise.

We denote the covariance matrices of \mathbf{a} and \mathbf{n} by \mathbf{C}_a and \mathbf{C}_w , respectively, where \mathbf{C}_w is diagonal (but not necessarily uniform), and \mathbf{C}_a is the covariance of the noise baseline amplitudes. If the noise is stationary, the latter is band-diagonal to a good approximation, and can be represented as a filter in Fourier domain. If the baseline length equals one TOI sample ($N_a = 1$), \mathbf{C}_a becomes equal to the time-domain covariance of the $1/f$ noise component. The construction of the covariance in the general case of $N_a > 1$ is presented in [Keihänen et al. \(2010\)](#); in this work we will assume $N_a = 1$.

In the following, both covariance matrices are assumed to be known a priori. Estimating the noise properties from the data itself (as part of the Gibbs sampling process) is addressed by [Ihle et al. \(2020\)](#).

We now proceed to write out the posterior distribution, $P(\mathbf{m}, \mathbf{a} | \mathbf{y}, \mathbf{C}_w, \mathbf{C}_a)$, for the (\mathbf{a}, \mathbf{m}) model, given some TOI data stream \mathbf{y} and assumed known noise properties. This is the posterior distribution we eventually want to sample by using Gibbs sampling technique, and may, according to Bayes’ theorem, be written as

$$P(\mathbf{m}, \mathbf{a} | \mathbf{y}, \mathbf{C}_w, \mathbf{C}_a) = P(\mathbf{y} | \mathbf{m}, \mathbf{a}, \mathbf{C}_w) \frac{P(\mathbf{m})P(\mathbf{a} | \mathbf{C}_a)}{P(\mathbf{y})}. \quad (3)$$

Here we have assumed that \mathbf{a} and \mathbf{m} are statistically independent, and we include \mathbf{C}_a and \mathbf{C}_w explicitly only in factors for which the conditional in question actually depends on them.

The denominator $P(\mathbf{y})$ is an overall normalization factor and can be ignored, since the methods we use for drawing samples from the likelihood are insensitive to the normalization. Furthermore, we assume a uniform prior for the sky map \mathbf{m} , $P(\mathbf{m}) = 1$, such that

$$P(\mathbf{m}, \mathbf{a} | \mathbf{y}, \mathbf{C}_w, \mathbf{C}_a) \propto P(\mathbf{y} | \mathbf{m}, \mathbf{a}, \mathbf{C}_w)P(\mathbf{a} | \mathbf{C}_a). \quad (4)$$

The first factor on the right is the probability of observing a data stream \mathbf{y} for given realization of correlated noise \mathbf{a} and for a given sky map \mathbf{m} . With both \mathbf{a} and \mathbf{m} fixed, the only difference between the model and the data comes from white noise. We

obtain this likelihood from the white noise distribution, which is assumed to be Gaussian with covariance \mathbf{C}_w ,

$$P(\mathbf{y} | \mathbf{m}, \mathbf{a}, \mathbf{C}_w) = \frac{e^{-\frac{1}{2}(\mathbf{y}-\mathbf{F}\mathbf{a}-\mathbf{P}\mathbf{m})^T \mathbf{C}_w^{-1}(\mathbf{y}-\mathbf{F}\mathbf{a}-\mathbf{P}\mathbf{m})}}{\sqrt{|\mathbf{C}_w|}}. \quad (5)$$

The second distribution on the right-hand side of Eq. (4) represents a prior on \mathbf{a} , i.e., the probability of obtaining a given realization of correlated noise in the absence of actual measurements. As is customary in *Planck* map-making, we assume that the correlated noise component also is Gaussian distributed, such that

$$P(\mathbf{a} | \mathbf{C}_a) = \frac{e^{-\mathbf{a}^T \mathbf{C}_a^{-1} \mathbf{a}}}{\sqrt{|\mathbf{C}_a|}}. \quad (6)$$

The conventional destriping procedure finds the combination (\mathbf{a}, \mathbf{m}) that maximizes the posterior distribution in Eq. (4). Equating the derivative of this expression with respect to (\mathbf{a}, \mathbf{m}) to zero leads to a large linear system, which can be solved by conjugate gradient iteration (see, e.g., Keihänen et al. 2010).

In this paper, we instead proceed to use Gibbs sampling to sample from the distribution in Eq. (4). One full Gibbs sampling step consists of two substeps, in each of which one of the two parameters \mathbf{m}, \mathbf{a} is kept fixed, and the other is drawn from the corresponding conditional distribution,

$$\begin{aligned} \mathbf{m}' &\leftarrow P(\mathbf{m} | \mathbf{a}; \mathbf{y}, \mathbf{C}_w) \\ \mathbf{a}' &\leftarrow P(\mathbf{a} | \mathbf{m}; \mathbf{y}, \mathbf{C}_w, \mathbf{C}_a) \end{aligned} \quad (7)$$

We use the semicolon to separated sampling parameters, which are however considered constant in the current sampling step, from parameters not sampled. Here the symbol “ \leftarrow ” indicates drawing a sample from the distribution on the right-hand side. Let us now look at these two substeps more closely:

1. For a given data stream \mathbf{y} and noise baselines \mathbf{a} , we update the sky map \mathbf{m} by drawing a sample from the Gaussian distribution

$$P(\mathbf{m} | \mathbf{a}; \mathbf{y}, \mathbf{C}_w) \propto \frac{e^{-\frac{1}{2}(\mathbf{y}'-\mathbf{P}\mathbf{m})^T \mathbf{C}_w^{-1}(\mathbf{y}'-\mathbf{P}\mathbf{m})}}{\sqrt{|\mathbf{C}_w|}} \quad (8)$$

where $\mathbf{y}' = \mathbf{y} - \mathbf{F}\mathbf{a}$ is the data stream from which we have subtracted the current \mathbf{a} sample. Thus \mathbf{y}' represents the current estimate of the noise-cleaned TOI stream.

2. For given data stream \mathbf{y} and sky \mathbf{m} , we update the baseline vector \mathbf{a}' by drawing a sample from the distribution

$$P(\mathbf{a} | \mathbf{m}; \mathbf{y}, \mathbf{C}_w, \mathbf{C}_a) \propto \frac{e^{-\frac{1}{2}(\mathbf{y}''-\mathbf{F}\mathbf{a})^T \mathbf{C}_w^{-1}(\mathbf{y}''-\mathbf{F}\mathbf{a})}}{\sqrt{|\mathbf{C}_w|}} \frac{e^{-\mathbf{a}^T \mathbf{C}_a^{-1} \mathbf{a}}}{\sqrt{|\mathbf{C}_a|}}, \quad (9)$$

where now $\mathbf{y}'' = \mathbf{y} - \mathbf{P}\mathbf{m}$ is a data stream from which we have subtracted the current \mathbf{m} sample. Thus \mathbf{y}'' represents the current estimate of the noise-only TOI stream.

The outcome from the sampling procedure is a chain of \mathbf{m} and \mathbf{a} samples, with their distribution sampling the combined likelihood of Eq. (4).

The conditional distributions in Eqs. (8) and (9) are both multivariate Gaussian distributions, from which samples may be drawn efficiently using standard methods; see, e.g., Appendix A in *BeyondPlanck Collaboration* (2020) and references therein. In the following, we briefly review the main steps for convenient reference purposes.

Consider a Gaussian distribution for a stochastic variable \mathbf{x} ,

$$P(\mathbf{x}) = \frac{e^{-\frac{1}{2}(\mathbf{y}-\mathbf{A}\mathbf{x})^T \mathbf{C}_n^{-1}(\mathbf{y}-\mathbf{A}\mathbf{x})}}{\sqrt{|\mathbf{C}_n|}} \frac{e^{-\frac{1}{2}\mathbf{x}^T \mathbf{C}_x^{-1} \mathbf{x}}}{\sqrt{|\mathbf{C}_x|}} \quad (10)$$

where \mathbf{y} represents data (observations); \mathbf{A} is some linear operator that connects the unknown \mathbf{x} to the data; \mathbf{C}_n is the noise covariance, which may or may not be diagonal; and \mathbf{C}_x is an optional covariance matrix for the prior of \mathbf{x} . The value of \mathbf{x} that maximizes the likelihood is readily found to be

$$\mathbf{x}_{\text{ML}} = (\mathbf{A}^T \mathbf{C}_n^{-1} \mathbf{A} + \mathbf{C}_x^{-1})^{-1} \mathbf{A}^T \mathbf{C}_n^{-1} \mathbf{y}. \quad (11)$$

Rather than finding the maximum-likelihood solution, we now want to draw a random sample of the distribution in Eq. (10). This can be done by solving a linear system similar to that of Eq. (11), but with a modified right-hand side \mathbf{b} , as

$$\begin{aligned} \mathbf{b} &= \mathbf{A}^T \mathbf{C}_n^{-1} \mathbf{y} + \mathbf{A}^T \mathbf{C}_n^{-1/2} \boldsymbol{\omega}_1 + \mathbf{C}_x^{-1/2} \boldsymbol{\omega}_2 \\ \mathbf{x} &= (\mathbf{A}^T \mathbf{C}_n^{-1} \mathbf{A} + \mathbf{C}_x^{-1})^{-1} \mathbf{b}. \end{aligned} \quad (12)$$

Here $\boldsymbol{\omega}_1$ and $\boldsymbol{\omega}_2$ are two vectors of random numbers drawn from a normalized Gaussian distribution $N(\mathbf{0}, \mathbf{I})$. The first vector has length equal to that of the data stream \mathbf{y} , the second one to that of \mathbf{x} .

We now want to apply this to our map-making problem. We take turns in drawing samples from the distributions of Eqs. (8) and (9). We end up with the following two-step procedure. Starting from sample (\mathbf{m}, \mathbf{a}) , we update the parameters as follows.

1. Map sampling (distribution of Eq. (8), no prior):

$$\mathbf{m}' = (\mathbf{P}^T \mathbf{C}_w^{-1} \mathbf{P})^{-1} [\mathbf{P}^T \mathbf{C}_w^{-1} (\mathbf{y} - \mathbf{F}\mathbf{a}) + \mathbf{C}_w^{-1/2} \boldsymbol{\omega}_1] \quad (13)$$

2. Noise sampling (Eq. (9)):

$$\begin{aligned} \mathbf{b} &= \mathbf{F}^T \mathbf{C}_w^{-1} (\mathbf{y} - \mathbf{P}\mathbf{m}') + \mathbf{F}^T \mathbf{C}_w^{-1/2} \boldsymbol{\omega}_2 + \mathbf{C}_a^{-1/2} \boldsymbol{\omega}_3 \\ \mathbf{a}' &= (\mathbf{F}^T \mathbf{C}_w^{-1} \mathbf{F} + \mathbf{C}_a^{-1})^{-1} \mathbf{b} \end{aligned} \quad (14)$$

To draw one pair of samples we thus need three independent Gaussian random vectors, $\boldsymbol{\omega}_1$, $\boldsymbol{\omega}_2$, and $\boldsymbol{\omega}_3$. Equations (13) and (14) summarize our Gibbs map-making algorithm.

2.2. Assumptions and optimization

The above discussion is general, and few assumptions regarding the experiment in question are made. However, to make the formalism more practical in terms of computer code implementation, we make a few assumptions that are familiar from the conventional *Planck* data processing pipeline:

1. We ignore beam smearing effects, and assume that all signal recorded by a detector at a time comes from the pixel where the beam center falls. We are regarding the beam smoothing as a property of the sky itself, an assumption which is strictly valid only for symmetric beams. Exact treatment of an asymmetric beam requires full beam deconvolution, which is beyond the scope of this paper. With this assumption, the pointing matrix \mathbf{P} is sparse, with three nonzero elements on each row, corresponding to three Stokes components of one pixel.
2. We do not correct for bandpass effects, and assume that all detectors see the same sky.

3. Detector noise is uncorrelated between pointing periods.
4. Correlated noise within a pointing period is Gaussian and stationary.
5. The white noise component, by definition, is uncorrelated from sample to sample, but not necessarily with constant variance. The covariance C_w is thus diagonal, but the values of the diagonal elements are allowed to vary. In the following we make the further simplifying assumption that the variance stays constant within one pointing period. However, we allow for the possibility that some of the samples are discarded from the analysis by setting $C_w^{-1} = 0$.

Under these assumptions, the coupling matrix $P^T C_w^{-1} P$ is block-diagonal, and consists of a 3×3 block per pixel that may be easily inverted. The map sampling step of Eq. (13) represents a simple binning operation, where the noise-cleaned TOI samples are coadded into pixels as given by the pointing matrix P , and the resulting map is normalized with the corresponding 3×3 matrix.

The noise sampling step can be carried out independently for each pointing period, which has an average length of about 40 minutes. This leads to a significant memory saving when compared to full map-making, and for the first time we can bring the baseline length down to one single sample. At this extreme limit F reduces to the identity matrix, $F = I$, and the noise sampling step of Eq. (14) simplifies to

$$\mathbf{b} = C_w^{-1}(\mathbf{y} - P\mathbf{m}') + C_w^{-1/2}\omega_2 + C_a^{-1/2}\omega_3 \quad (15)$$

and

$$\mathbf{a}' = (C_w^{-1} + C_a^{-1})^{-1}\mathbf{b}. \quad (16)$$

Here the term $C_a^{-1}\omega_3$ represents the operation of applying the noise filter to a sequence of Gaussian random numbers. Since C_a is stationary, this can be carried out efficiently with FFT technique.

To increase the efficiency of the FFT operations, it is useful to pad the data to a suitable FFT length. In this paper, we have chosen the following procedure to deal with data ends: To reduce boundary effects, we first subtract the mean of the data (over unflagged samples), and only then pad the data with zeroes to a suitable FFT length. We then carry out the FFT operation; apply the relevant filter; perform the inverse FFT; cut off the padded region; and add back the original offset.

2.3. Flagging and masking

As mentioned regarding Eq. (16), C_a^{-1} represents a stationary filter. However, the presence of missing observations makes the full coupling matrix $C_w^{-1} + C_a^{-1}$ non-stationary. The two most common causes for missing observations are glitches in the data collection, and the application of an analysis mask that excludes bright foreground regions on the sky, which is useful to prevent striping along the scanning path of the instrument.

The most convenient way of implementing masking is formally by setting the white noise level to infinity for the discarded samples, or, equivalently, $C_w^{-1} = 0$. The computational price for this is that Eq. (16) can no longer be treated as a strict Fourier filter. The system can still be solved through conjugate gradient iteration, but this is significantly slower than solving the stationary system. A faster, but approximate, solution is to fill the gaps with a simulated data. We consider both options more closely in the following.

2.3.1. Solving the non-stationary system

We first consider the exact solution of the non-stationary system in Eq. (16), where $C_w^{-1} = 0$ in the flagged part of the data. Let us for convenience define

$$\mathbf{A} = C_w^{-1} + C_a^{-1}, \quad (17)$$

and \mathbf{M} to be a stationary version of the same, with flags appropriately omitted,

$$\mathbf{M} = I/\sigma^2 + C_a^{-1}. \quad (18)$$

If only a small fraction of samples are flagged, we have

$$\mathbf{M}^{-1}\mathbf{A} \approx I. \quad (19)$$

Conjugate gradient iteration can be sped up significantly with a properly chosen preconditioner matrix. In our case, \mathbf{M} represents a natural choice for a preconditioner. However, even with preconditioning, full convergence typically requires 40–50 iteration steps, which becomes computationally prohibitive when this algorithm is repeated within every Gibbs loop.

Fortunately, we can speed up the procedure significantly by reformulating the problem as follows. We first symbolically write the right-hand side of Eq. (16) in the form

$$\mathbf{A}^{-1}\mathbf{b} = \mathbf{M}^{-1}\mathbf{b} + \text{correction}. \quad (20)$$

Second, we define

$$\mathbf{D} = I/\sigma^2 - C_w^{-1} \quad (21)$$

to be the deviation from the constant white noise variance in C_w . Explicitly, \mathbf{D} is a diagonal matrix with zero on the diagonal for the non-flagged samples, and $1/\sigma^2$ for the flagged ones. We denote by the number of flagged samples on the pointing period by N_f , and the total number of samples by N_s . Typically, only a small fraction of samples are flagged, and thus N_f is much smaller than N_s . We then eigenmode decompose \mathbf{D} into $\mathbf{D} = \mathbf{U}\delta\mathbf{U}^T$, where now δ is a diagonal matrix of size (N_f, N_f) with $1/\sigma^2$ on the diagonal. The matrix \mathbf{U} has size (N_s, N_f) , and each column of \mathbf{U} corresponds to one flagged sample, and contains one nonzero (equal to one) element marking its position on the data stream.

Using this notation we have

$$\mathbf{A} = C_w^{-1} + C_a^{-1} = \mathbf{M} - \mathbf{U}\delta\mathbf{U}^T. \quad (22)$$

Using the well-known Woodbury matrix identity we can re-write the matrix inverse into the form

$$\mathbf{A}^{-1} = \mathbf{M}^{-1} + \mathbf{M}^{-1}\mathbf{U}(\delta^{-1} - \mathbf{U}^T\mathbf{M}^{-1}\mathbf{U})^{-1}\mathbf{U}^T\mathbf{M}^{-1}. \quad (23)$$

The solution of Eq. (16) therefore becomes

$$\mathbf{a}' = \mathbf{M}^{-1}\mathbf{b} + \mathbf{M}^{-1}\mathbf{U}(\sigma^2\mathbf{I} - \mathbf{U}^T\mathbf{M}^{-1}\mathbf{U})^{-1}\mathbf{U}^T\mathbf{M}^{-1}\mathbf{b} \quad (24)$$

where we have written $\delta^{-1} = \sigma^2\mathbf{I}$. This expression conforms to the format of Eq. (20), and is the solution we were aiming at.

The vector \mathbf{a}' can now be computed efficiently from Eq. (24). The first term, $\mathbf{M}^{-1}\mathbf{b}$, represents the operation of applying the stationary filter of \mathbf{M} to the right-hand side \mathbf{b} , and can be carried out efficiently by FFT techniques. The rest represents a correction that takes care of flagging. Working from right to left, the matrix \mathbf{U}^T represents the trivial operation of picking the flagged samples from a full TOI, and concatenating them into a vector of length N_f . The middle matrix inversion must still be carried out using conjugate gradient iteration, but the system is now much smaller than the original one. Finally, the matrix \mathbf{U} represents the operation of inserting the N_f values of its target vector into a full-size TOI, in the positions of the flagged samples. We find that the solution of Eq. (24) requires only 5–6 iteration steps for convergence, to be contrasted with 40–50 steps required for the original system to converge.

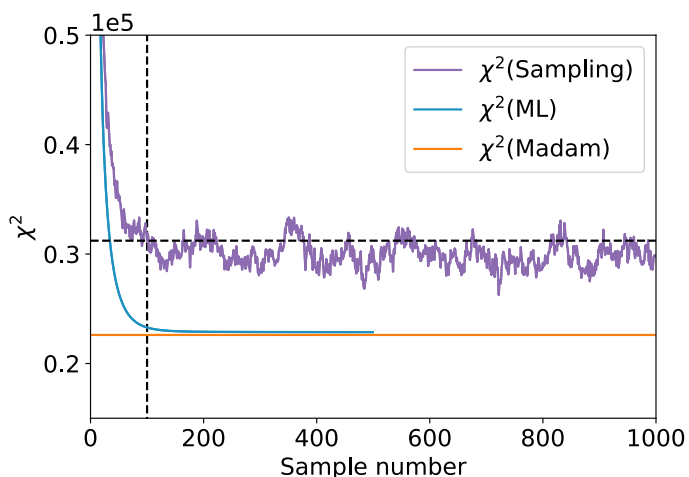


Fig. 1. Gibbs chain burn-in as illustrated by the χ^2 difference between a given Gibbs sample and the noise-free reference map. The dashed line shows the χ^2 level after 100 steps. The χ^2 value from Madam is shown by a horizontal line.

2.3.2. Gap filling

As efficient as the procedure presented above is, solving the full exact and non-stationary system still implies a computational cost that is 5–6 times higher compared to a case where no flagging is applied. In the following we therefore present an alternative way of handling the flagged data sections: we fill them with a noise realization, as part of the overall Gibbs sampling procedure. We note that similar gap filling techniques have been routinely used by a long history of previous CMB experiments, including *Planck* LFI (e.g., [Planck Collaboration II 2014](#)), and we will in the following discuss both exact and approximate solutions to this problem.

First, we introduce the white noise component \mathbf{w} in the flagged section as a new explicit Gibbs variable to be sampled over. The original noise sampling step,

$$\mathbf{a}' \leftarrow P(\mathbf{a} \mid \mathbf{m}; \mathbf{y}, \mathbf{C}_x), \quad (25)$$

is therefore replaced by a two-step procedure

$$\begin{aligned} \mathbf{w}' &\leftarrow P(\mathbf{w} \mid \mathbf{C}_w) \\ \mathbf{a}' &\leftarrow P(\mathbf{a} \mid \mathbf{m}, \mathbf{w}; \mathbf{y}, \mathbf{C}_x). \end{aligned} \quad (26)$$

The first step consists of generating a white noise sample for all flagged TOI segments, which is simply equivalent to drawing a random realization from the Gaussian distribution with variance $\mathbf{C}_w = \sigma^2 \mathbf{I}$. The second step represents the usual sampling operation of Eqs. (15) and (16), but this time for a full data stream where the gaps are filled, and consequently, the white noise covariance \mathbf{C}_w is uniform.

The remaining question is, what should go in place of $\mathbf{y} - \mathbf{P}\mathbf{m}'$ in Eq. (15)? This vector represents the current best estimate of the noise stream, including both correlated and white noise. In the non-flagged data section, it is therefore raw data minus the sky estimate, as usual. In the flagged section, where no information is available from the data regarding \mathbf{y} , it is given by the correlated noise TOI, \mathbf{a} , from the preceding Gibbs iteration plus the white noise realization \mathbf{w} just generated. With the gaps filled in this manner, the calculation of Eq. (16) can be solved with FFT technique without CG iteration, and the overall algorithm therefore becomes very fast.

This solution has two potential disadvantages compared to the original solution, worth keeping in mind. The first is a longer

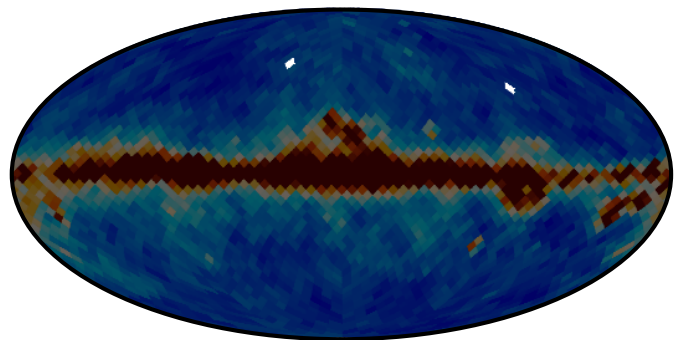


Fig. 2. Location of HEALPix $N_{\text{side}} = 16$ pixels 200 and 600 on the sky in nested ordering. The colour scale of the underlying map is dimmed to highlight the locations of the two pixels.

overall Monte Carlo correlation length, which arises from the fact that we are now conditionally sampling the correlated and white noise terms separately, which is always less efficient than sampling them jointly. The second disadvantage is the fact that this method increases the overall memory requirements, since the correlated noise TOI for the flagged section also have to be stored in memory between two consecutive Gibbs iterations. We test both solutions with simulations.

3. Simulations

We characterize and validate the algorithms described above using controlled simulated data. Specifically, we create a set of simulated time-ordered data using the *Level-S* simulation software ([Reinecke et al. 2006](#)). We choose to focus on the *Planck* LFI 30 GHz channel, since the data set for this particular channel is the smallest of the *Planck* channels in terms of data volume, and therefore also has the fastest turnaround time. The simulated data span the full *Planck* LFI mission, i.e., four years of observations.

The simulated data contain time streams for CMB, foregrounds, and noise. We simulate each component separately, and use the sum of all time streams as an input to the Gibbs map-maker. The CMB signal is simulated based on theoretical angular power spectra, while the foreground model is adopted from a preliminary *BEYONDPLANCK* analysis, taking into account radiometer-specific beam and bandpass responses. Both CMB and foreground simulations contain real *Planck* main and intermediate beams, as described by [Planck Collaboration IV \(2016\)](#). We use *convigt* ([Prézeau & Reinecke 2010](#)) and *multimod* tools from the *Planck Level-S* package to convolve the sky with the beam, and to scan a time-ordered data stream from the input sky according to the detector pointing. The noise TOI is simulated based on realistic noise parameters, as described by [Planck Collaboration II \(2016\)](#), and generated with *multimod*.

The *Planck* LFI detector pointing is regenerated with *Level-S*, and has been confirmed to agree well with the real *Planck* LFI pointing. Additionally, we use actual *Planck* LFI flags to discard flagged samples, and a processing mask described by [Suur-Uski et al. \(2020\)](#) to mask out regions with strong gradients.

In addition we generate a set of 101 noise realizations by creating a noise TOD with *Level-S* and calculating corresponding maps with *Madam*. We use this set of maps to study potential noise biases. The noise realization used in the main validation work of the Gibbs sampler is the first noise MC sample. Hence we have a total of 102 noise realizations.

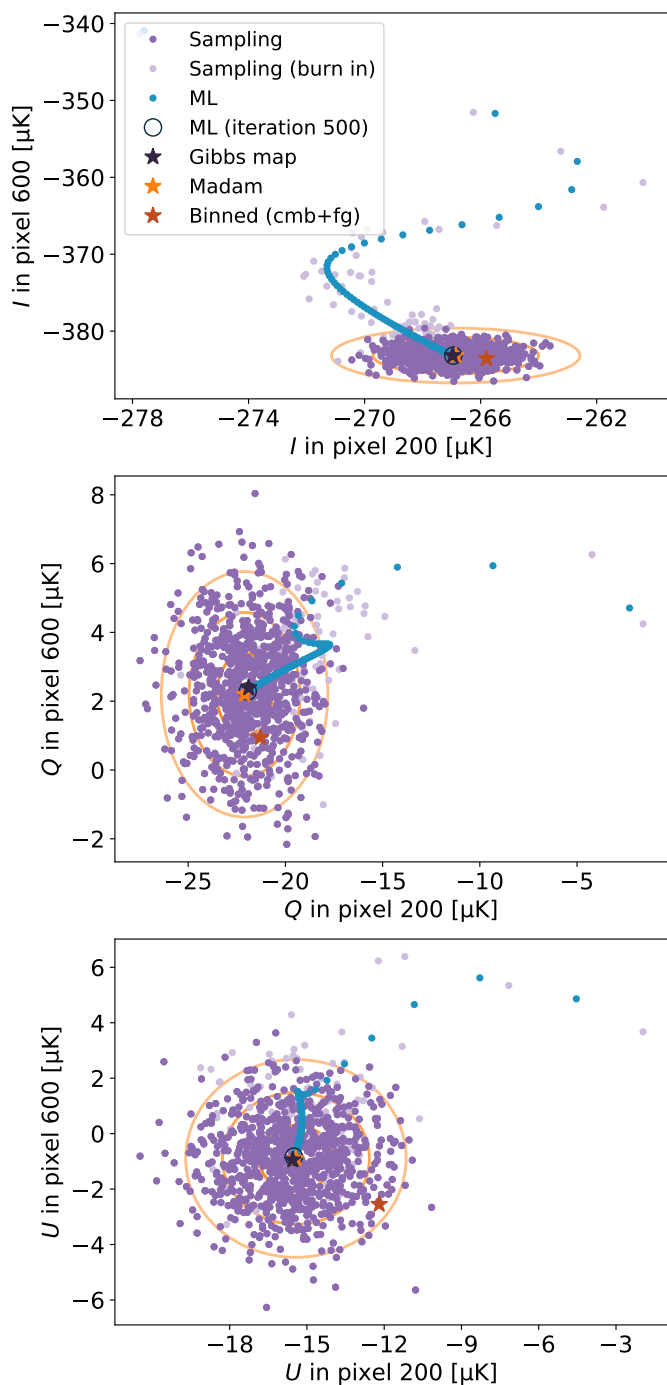


Fig. 3. Gibbs chains for the Stokes parameters I , Q and U in pixels 200 and 600 in a HEALPix $N_{\text{side}} = 16$ map with nested ordering. The value in pixel 600 is shown on the y-axis, plotted against the value in pixel 200 (x-axis). Purple dots indicate individual steps during a sampling run, while blue dots indicate steps in a maximum-likelihood run. The orange stars indicate the Madam solution, and orange contours indicate confidence regions based on white noise uncertainties alone.

4. Results

We now run the Gibbs sampling map-making algorithm described in Sect. 2 on the simulation data described in Sect. 3. As already mentioned, we use a test code for this purpose that is independent of the Commander code that is employed for the full BEYONDPLANCK analysis, as summarized by BeyondPlanck Collaboration (2020). This allows us to examine the map-making

problem in isolation, and also to try out different approaches with a faster turn-around time. The test code implements the Gibbs sampling map-making procedure, as presented in Sect. 2, without any component separation step. The output maps thus contain both the CMB and foreground signal, and represent traditional frequency maps, rather than astrophysical component maps.

We run the code both in “sampling mode” and in “maximum-likelihood mode”. In the sampling mode, the code performs full Gibbs sampling, and draws samples from the combined baseline-plus-map posterior distribution. In the maximum-likelihood mode, the fluctuation terms that involve ω_1 , ω_2 , and ω_3 in Eqs. (13) and (14) are omitted, with the effect that the algorithm performs a (computationally very inefficient) steepest-descent search towards the maximum-likelihood solution.

In the following, we refer to the posterior mean map, as evaluated from the mean of the ensemble of posterior samples, as the “Gibbs map”, with a burn-in period appropriately excluded. Thus, the Gibbs map represents a single-point estimate of the true map. In contrast, the “maximum-likelihood map” refers to the last sample of a chain with the sampling terms disabled.

Unless stated otherwise, we fill the gaps as described in Sect. 2.3.2, using the previous correlated noise sample as baseline. In the noise sampling step, we mask the Galactic region to reduce leakage of strong foreground signal into polarization. The mask is applied only in the noise sampling step, while in the map-binning step, all data are included, such that a full-sky map is produced as output. We briefly discuss the other option, exact solution of the non-stationary system, in section 4.3.

Because we are working with simulated data, we know exactly what the true sky signal should be. As a reference, we therefore construct a map from the pure CMB-plus-foreground time stream, and exclude both correlated and white noise. We refer to this ideal map as the “noise-free map”, which represents the map we would obtain in the absence of instrumental noise. The difference between the Gibbs estimates and this map provides a measure of residual noise in the former.

We construct another validation reference by running the Madam map-making code on the same simulated data. Madam, and the new Gibbs sampler when run in the maximum-likelihood mode, solve essentially the same likelihood problem, though through a different implementation. We thus expect the results to be very close, if not identical. Small differences may arise due different baseline lengths, or from different implementation of the noise filter, or simply from different convergence properties. In particular, since a Gibbs sampler only allow changes along coordinate directions, we expect this approach to converge much slower towards the maximum-likelihood solution than a conjugate gradient solver like Madam. We note, however, that the Gibbs sampling approach will normally not be used in the maximum-likelihood mode, but rather as a sampler within a more complete analysis framework.

4.1. Pixel space

We begin by inspecting the maps visually. Figure 1 shows the unnormalized χ^2 difference, computed as the squared difference between the noise-free map and a map from the Gibbs chain, as a function of sample number. For each map we first subtract the mean of I to remove arbitrary map offsets. This applies for all maps in this paper’s analysis. We interpret the first 100 steps as the “burn-in” period, and discard them from all further analysis. In the maximum-likelihood mode, the χ^2 value converges towards the Madam value, shown by a horizontal line. In the sam-

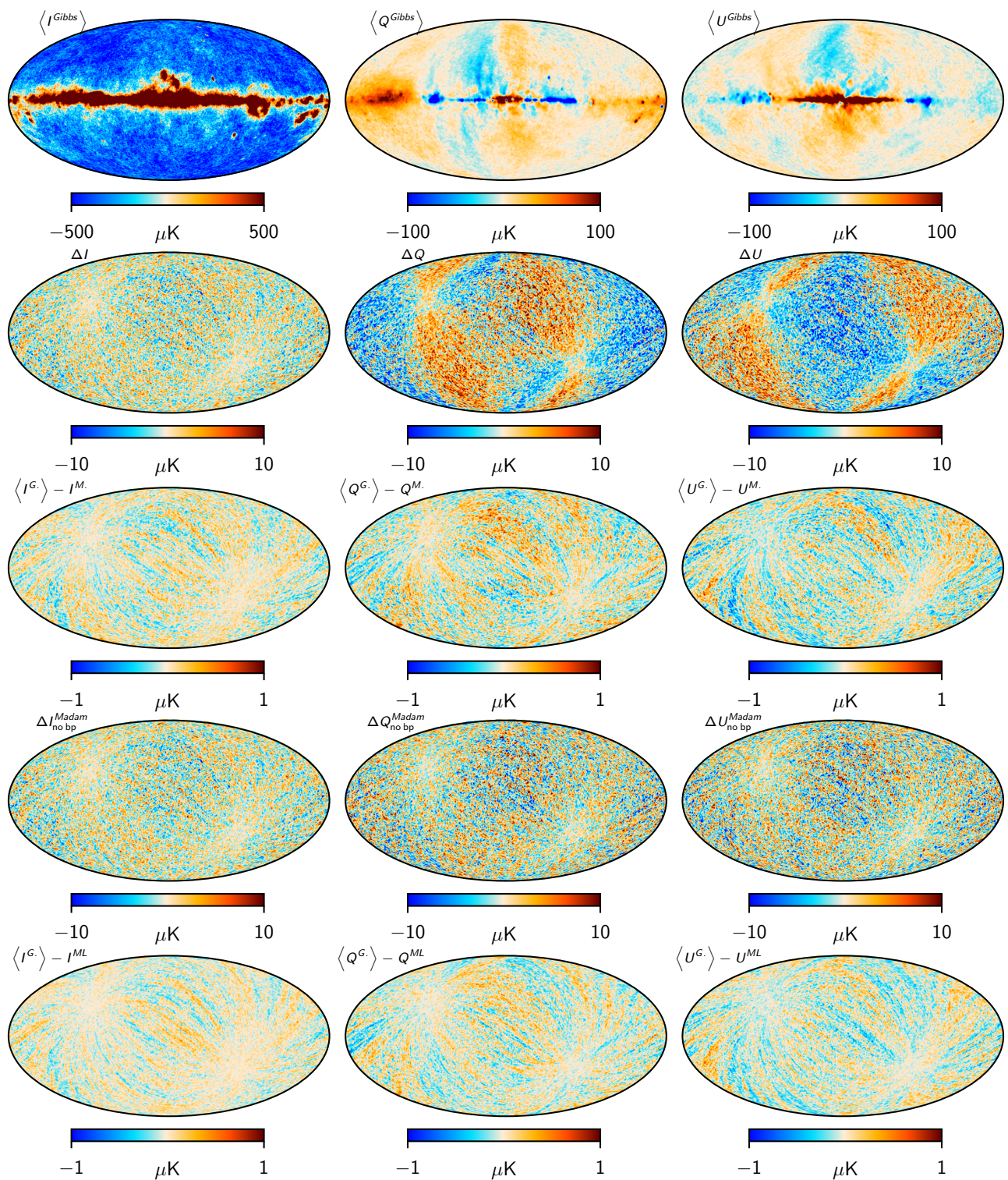


Fig. 4. Temperature and polarization maps from simulation. Columns show, from left to right, the Stokes T , Q , and U components. Rows show, from top to bottom, 1) Gibbs map: the mean of maps from the Gibbs chain, as evaluated from 900 samples; 2) absolute residual error as evaluated as the difference between the Gibbs map and the noise-free map; 3) the difference between the Gibbs map and the Madam map derived from the same data set; 4) residual error in Madam for a simulation that does not contain bandpass (*simulation that has same input foreground map for all radiometers*) evaluated as the difference between the Madam map and noise-free map; and 5) the difference between the Gibbs map and the maximum-likelihood map.

pling mode, the χ^2 value includes the additional variation from the sampling.

We now pick two sky pixels for closer examination. We arbitrarily select two pixels at resolution $N_{\text{side}} = 16$ from the region excluding strong foregrounds, with pixel indices 200 and 600 in

the HEALPix nested pixelization scheme; the locations of these pixels are indicated in Fig. 2, where they are shown on top of the simulated CMB+foreground map.

In Fig. 3 we plot the I, Q, U Stokes components of pixel 600 against those of pixel 200. This creates a two-dimensional

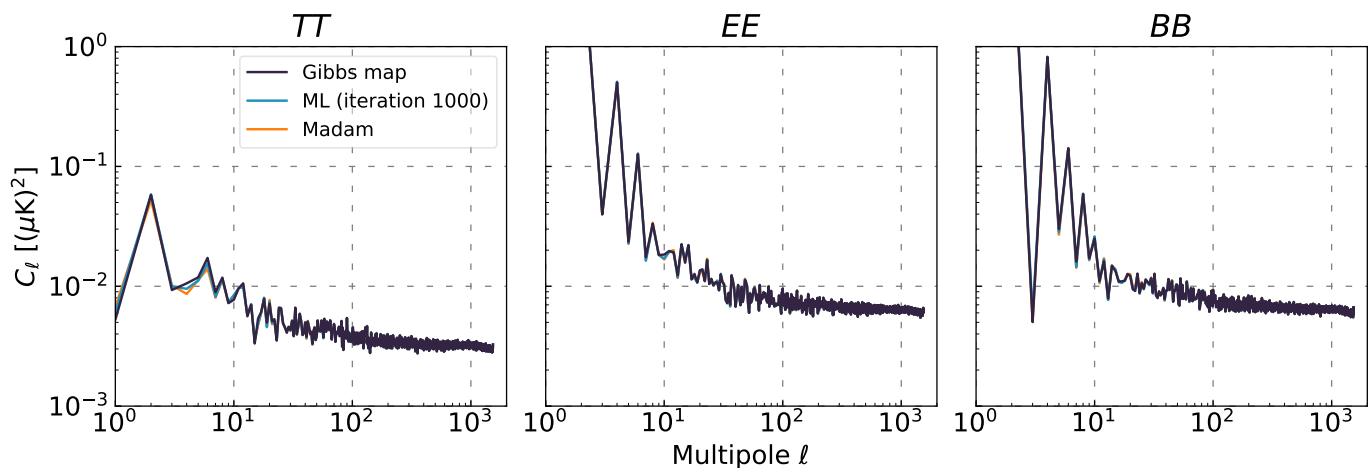


Fig. 5. Residual noise spectra for different map-making options. The residual noise spectrum is computed as the angular power spectrum of the residual noise map, which in turn is obtained as the difference between a map estimate and the noise-free map.

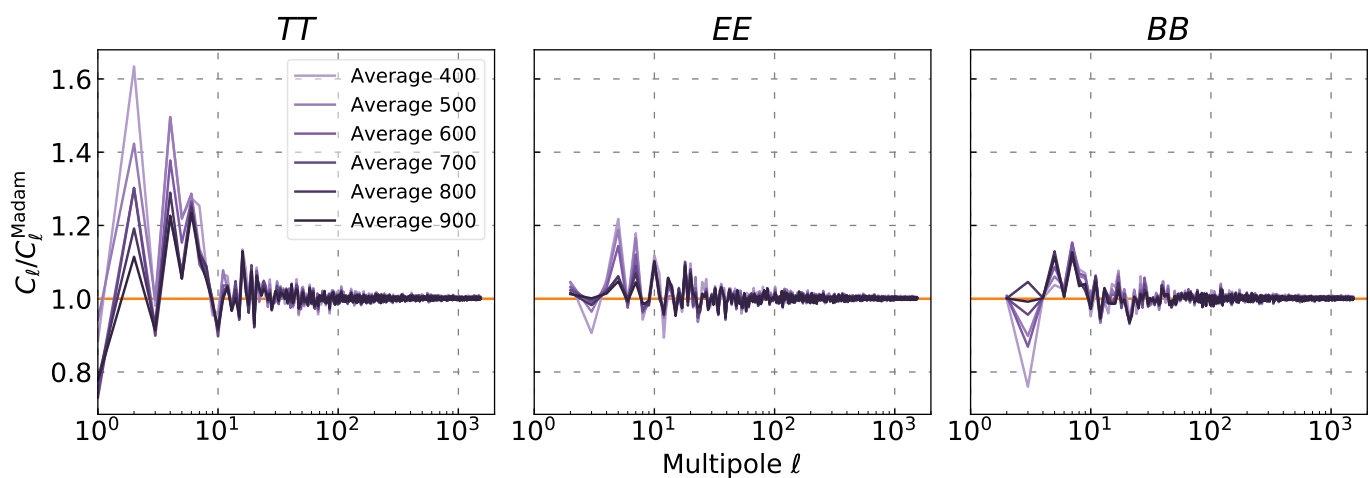


Fig. 6. Ratio of the residual noise spectrum of the Gibbs map to that of Madam, for different chain lengths.

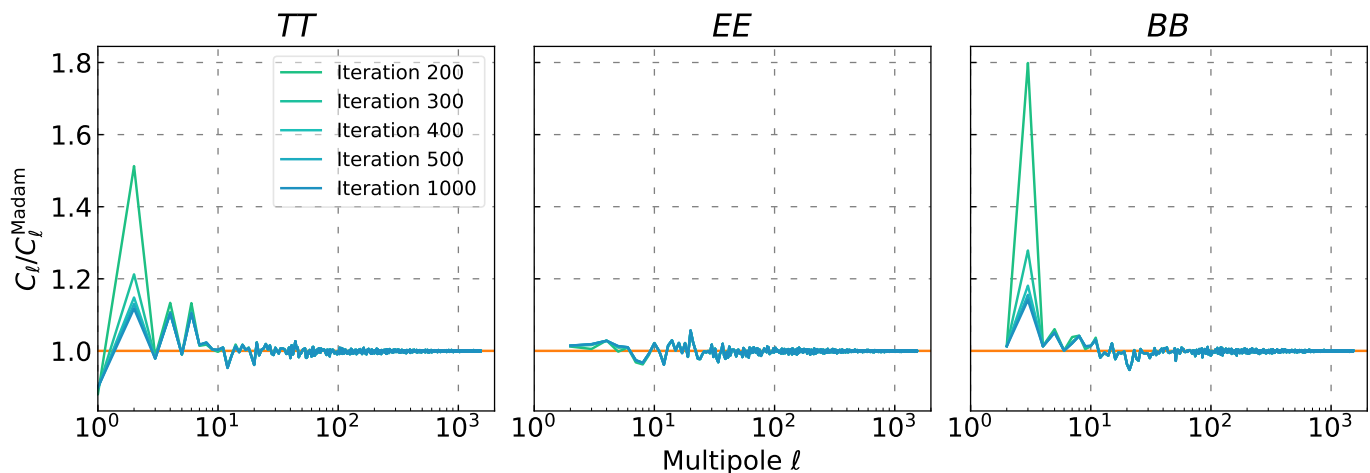


Fig. 7. Ratio of the residual noise spectrum of the maximum-likelihood map to that of Madam, for different Gibbs chain lengths.

plot that illustrates the behaviour of the Gibbs sampling chain. The correct signal value, as taken from the noise-free map, is indicated by a red star. The estimated values necessarily differ from this due to noise. The Madam estimate, representing the maximum-likelihood solution, is shown by an orange star. As expected, the Gibbs sampler in the maximum-likelihood mode

approaches the same solution, although we note that the number of steps required to reach it is large.

In the sampling mode, the map samples fluctuate around the maximum-likelihood solution, revealing the shape of the likelihood distribution. This can be compared to the theoretical white noise distribution. Along with the maximum-likelihood solution

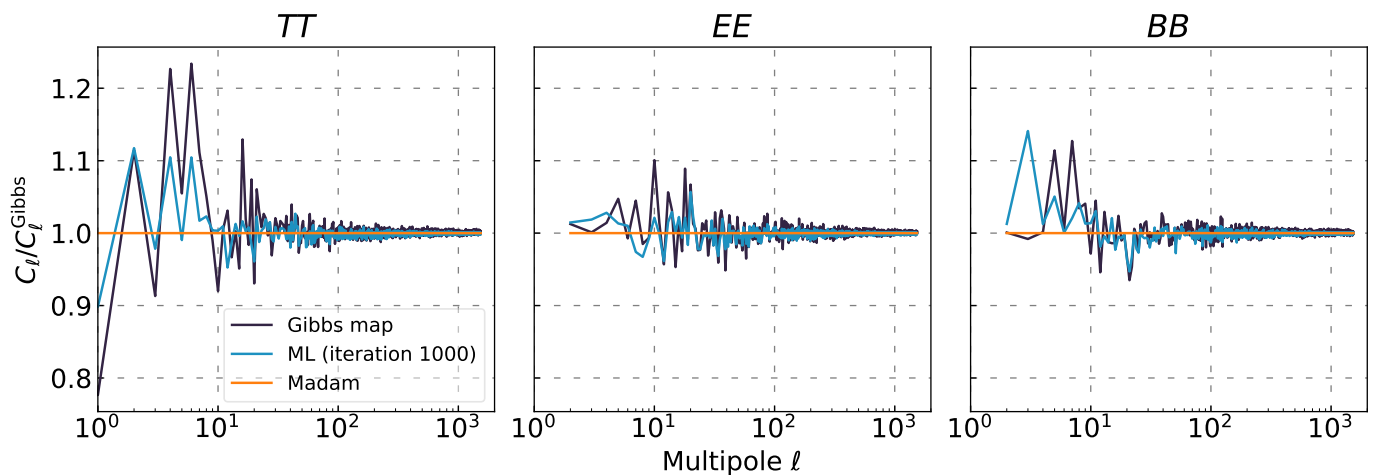


Fig. 8. Ratio of residual noise spectrum to that of Madam, for a Gibbs map and for a maximum-likelihood map with the largest available number of samples. The data are the same as in Figs. (6) and (7).

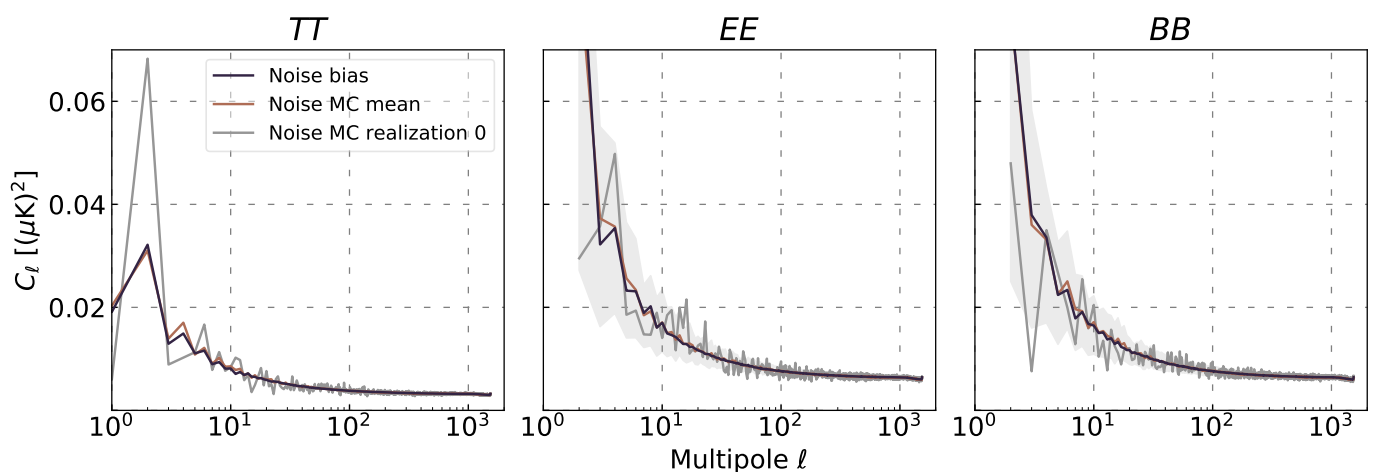


Fig. 9. Noise bias from Gibbs chain compared with noise Monte Carlo. Noise MC contains 101 realizations, processed with Madam. The mean of the MC spectra is plotted in brown, and $\pm 1\sigma$ regions in light grey. Realization 0 of noise MC is plotted in medium grey.

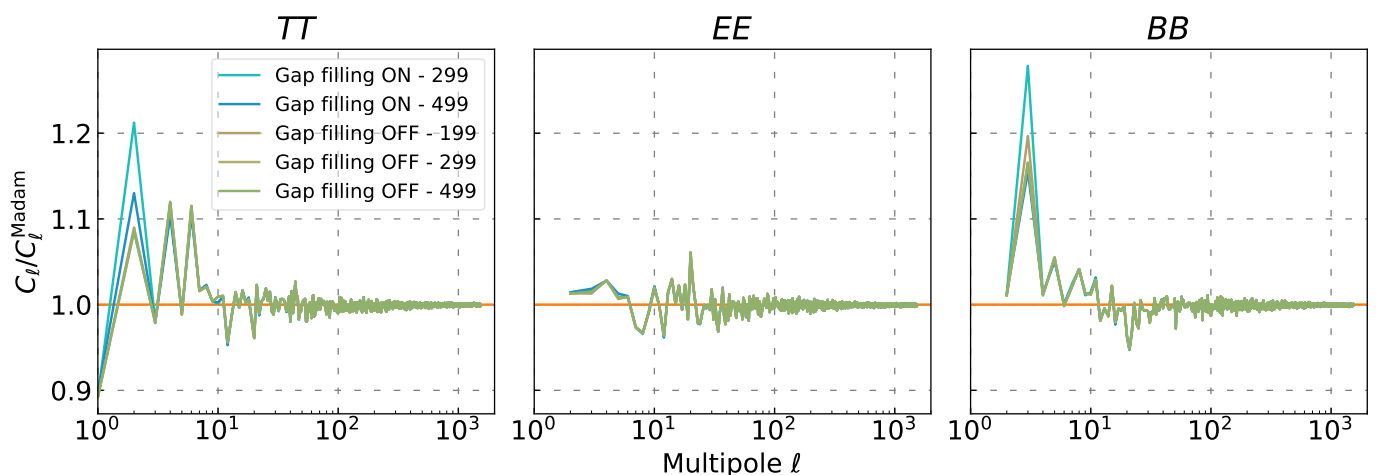


Fig. 10. Ratio of residual noise spectrum to that of Madam, with and without gap filling, for 199, 299, or 499 samples.

for the map, Madam produces a white noise approximation of the noise covariance. This is indicated by orange circles in the same plot. The Gibbs chain tracks the shape of the distribution well, when the burn-in period (shown by gray dots) is discarded. The sampled distribution includes also a contribution from correlated

noise, which is missing in the white noise estimate. As the residual is dominated by white noise, however, these are difficult to discern in the pixel plot. In Sect. 4.2 we will further examine the noise residuals in harmonic space, where correlated residuals are visible much more clearly.

The Stokes components (I, Q, U) of the pixelized Gibbs map are shown in the uppermost panel of Fig. 4, adopting a HEALPix resolution of $N_{\text{side}} = 512$, or $7'$ pixel size. All polarization components in this figure have been smoothed with a 1 deg FWHM Gaussian smoothing window to reduce noise.

The second row of Fig. 4 shows the difference with respect to the noise-free map. This represents residual noise and systematic errors in the Gibbs map. We observe that, in addition to white noise, there is also a large-scale signal residual in the polarization component, indicating leakage of temperature signal into polarization. However, when we take the difference between the Gibbs map and the Madam map constructed from the same data, the structure nearly disappears, as shown in the third row. This indicates that the same signal residual is present in the Madam map as well. The leakage is thus not a property of the Gibbs sampling method, but a feature common all map-making methods.

As shown below, the source of the leakage is detector-dependent bandpass and beam mismatch, coupled to a frequency-dependent foreground signal. To mitigate this, we have masked the Galactic region during correlated noise estimation. However, the mask size is a trade-off: removing more of the foreground will reduce the leakage, but at the same time will also remove useful data and make noise reduction more difficult. Here, we are working with the 30 GHz channel, which is particularly cumbersome in this respect, as the foreground signal extends over a large part of the sky.

To pinpoint the origin of the large-scale residual in the second row, we create a simplified simulation data set where the bandpasses of all radiometers are set equal. To do this, we took the bandpass-weighted input sky for radiometer LFI27M, and fed it as input to all radiometers, however always convolving with each radiometer's own beam. Since running a full Gibbs chain is computationally expensive, and we know that Madam is subject to same leakage, we only run Madam on the new simulation. The difference between the Madam map and the noise-free reference map is shown in fourth row of Fig. 4. The structure is strongly reduced as compared to the one seen in the second row. This shows that the large-scale structure seen in row 2 is caused by foreground signal residuals in combination with differential instrument responses, and associated with bandpass mismatch. This highlights the importance of combined map-making and systematics corrections, as discussed by [BeyondPlanck Collaboration \(2020\)](#), and accounting for these types of effects is one of the main motivations for the full BEYONDPLANCK Gibbs sampler.

Finally, in the bottom row of Fig. 4 we show the difference between the Gibbs map (with sampling), and the maximum-likelihood map (last sample from the Gibbs chain with sampling off). The differences between the two are below the $1 \mu\text{K}$ level.

4.2. Harmonic space

We now proceed to examine the noise residuals in harmonic space, where the correlated residuals are seen more clearly. In Fig. 5 we plot the residual noise spectrum for Madam, maximum-likelihood map, and the Gibbs map. The residual noise spectrum is computed as the angular power spectrum of the difference map between a map estimate and the noise-free map. All three spectra are very close to each other.

To show the differences more clearly, we plot ratios of these spectra in Figs. 6 and 7. We use the Madam spectrum as a reference, and plot the ratio of other spectra to it. In Fig. 6 we show the residual noise in the Gibbs map, for different numbers of sampling steps. In each case, the map is an average of the Gibbs

samples over the indicated number of samples. The burn-in period is excluded in all cases. The spectrum is very close to that of Madam at high multipoles, but differences are seen at the lowest multipoles. In particular, we see that the Gibbs map converges very slowly with number of iterations, resulting in an overall high computational cost. Clearly, a direct solver is highly preferred over the Gibbs approach in applications that only require a single maximum-likelihood solution, and no error estimate, as for instance is the case in most forward simulation-based analysis pipelines.

One could have hoped for the Gibbs map to yield a lower noise residual, due to the shorter baseline length. However, we do not observe this in our simulations. This is good news for the official *Planck* analysis, since it indicates that correlated noise at scales below the Madam baseline length (0.25 s) is already negligible. For a few multipoles ($\ell = 4 - 6$) Madam yields a lower residual than the Gibbs solver. This can be attributed to numerical differences in the implementation of the noise filter, and is well below the sample variance.

In a similar manner, Fig. 7 shows the ratio of residual noise spectrum in the maximum-likelihood map to that of the Madam map. Here, the map in question is the last sample of a Gibbs chain with the given number of steps, with sampling turned off. We see that more than 500 steps are required for convergence. In Fig. 8 we show in the same plot the residual spectra from Figs. 6 and 7. From both plots, we pick the result with highest number of samples.

For the Gibbs sampling approach, the scatter of the samples around the mean estimate provides a direct account of the residual noise, and may be used to construct an estimate of the noise bias as follows: We first compute individual noise maps by subtracting the average map from each map sample. We then compute the angular power spectrum of each noise map with the standard *anafast* tool ([Górski et al. 2005](#)), and obtain the noise bias as the mean of these spectra, dividing by $N - 1$ as usual for a variance estimate.

In Fig. 9 we plot this estimated noise bias together with the average noise spectrum from 101 noise-only Monte Carlo samples, as processed through Madam. The first MC sample is shown in dark grey, and represents the same data set as the one used in the validation of the Gibbs sampler. The noise bias and the Monte Carlo average agree very well. We see also that the differences seen in Fig. 8 at low multipoles are small compared with the random scatter between realizations in the noise MC.

Note that unlike the residual noise spectra that require information on the simulation input, the noise bias can be computed from Gibbs chains alone, since it involves only the Gibbs samples and their mean. The procedure is thus available when processing actual measurement data.

4.3. Computational costs

We run the simulation on a 24-core compute node with Intel Xeon E5-2697 (2.7 GHz) processors. On this system, one Madam run on the simulation data set takes 4000 seconds of wall time (27 core-hours). One Gibbs sampling step with gap filling takes 173 seconds, while the full cost of a Gibbs chain with 1000 steps is 1150 core-hours (2 days wall-clock time), or more than 40 times the cost of a Madam run. In maximum-likelihood the process is somewhat faster, taking 107 second per iteration, and a total of 360 core-hours for 500 iteration steps; this is still 13 times the cost of Madam. It is thus evident that if one is interested only in the maximum-likelihood solution, the Gibbs procedure is not competitive with more direct methods, such as Madam.

We have also tried running Gibbs sampling without gap filling, which is the most time-consuming step in the procedure, as it requires a conjugate gradient iteration inside every Gibbs step. Since we are dealing here with a full-scale simulation with foreground signal and bandpass effects, the convergence is somewhat slower than what we observed with the pure noise simulation of Sect. 2.3.1. The procedure takes 1814 seconds per Gibbs iteration, and is thus more than ten times slower than the procedure with gap filling. In our test case, the additional memory requirement associated with the gap filling procedure is negligible in comparison with the overall memory requirement.

In Fig. 10 we compare the residual noise as estimated both with gap filling and with the conjugate gradient solution, both in the maximum-likelihood mode. The conjugate gradient option does converge faster, but the differences are in the end negligible.

The most computationally expensive combination is the sampling mode without gap filling. Preliminary tests indicate that this option would take two weeks of wall-clock time, most likely without offering any benefit over the options already studied. Thus we do not examine this combination further.

5. Conclusions

We have introduced Gibbs sampling as a novel solution to the map-making problem for CMB experiments. Gibbs map-making can be run in “maximum-likelihood mode” to find the map solution that maximizes the likelihood function, or in “sampling mode” in which case the algorithm draw samples from the corresponding posterior distribution. The mean of this distribution gives a best estimate of the underlying true sky, while the scatter of the samples provides an account of the residual noise in the map estimate.

To validate the procedure, we have compared the results against those of a direct maximum-likelihood solver (*Madam*). We have demonstrated that with noise sampling disabled, the Gibbs sampling procedure can be used to find the maximum-likelihood map solution. Since the sampler proceeds in small one-dimensional steps through the large multi-dimensional parameter space, the procedure is relatively slow, and offers little benefit over direct methods. Even so, this is an important validation step.

The true value of the Gibbs sampling approach lies in error propagation and integration with systematic corrections. In this paper, we have demonstrated the first part, namely that Gibbs sampling provides an efficient method to sample the full likelihood distribution surrounding the maximum-likelihood map. This way we obtain a reliable estimate the level of residual noise in the map (noise bias), which is otherwise possible only through the construction of a pixel-to-pixel noise covariance matrix, which is notorious as a computationally demanding task, or through Monte Carlo simulations.

We have studied two ways to deal with gaps in the data: either solving an exact maximum-likelihood system where flagged samples are assigned an infinite variance, or including the gaps in the Gibbs process as another variable to sample. The latter translates into filling the gaps with a new white noise realization at every step. In our test case, gap filling turns out to be significantly more efficient, and is thus our method of choice. It is worth bearing in mind, however, that gap filling comes with an increased memory requirement, which may become prohibitive in other user cases.

The full power of Gibbs sampling as a map-making solution is realized in cases where map-making and noise removal are included as a part of a full Gibbs sampling machinery, including

foreground modeling and estimation of instrument effects. This is the goal of the larger *BEYONDPLANCK* project.

Acknowledgements. We thank Prof. Pedro Ferreira for useful suggestions, comments and discussions, and Dr. Diana Mjaschkova-Pascual for administrative support. We also thank the entire *Planck* and *WMAP* teams for invaluable support and discussions, and for their dedicated efforts through several decades without which this work would not be possible. The current work has received funding from the European Union’s Horizon 2020 research and innovation programme under grant agreement numbers 776282 (COMPET-4; *BEYONDPLANCK*), 772253 (ERC; *BITS2COSMOLOGY*), and 819478 (ERC; *COSMOGLOBE*). In addition, the collaboration acknowledges support from ESA; ASI and INAF (Italy); NASA and DoE (USA); Tekes, Academy of Finland (grant no. 295113), CSC, and Magnus Ehrnrooth foundation (Finland); RCN (Norway; grant nos. 263011, 274990); and PRACE (EU).

References

- Ashdown, M. A. J., Baccigalupi, C., Balbi, A., et al. 2007a, *A&A*, 471, 361
 Ashdown, M. A. J., Baccigalupi, C., Balbi, A., et al. 2007b, *A&A*, 467, 761
 Ashdown, M. A. J., Baccigalupi, C., Bartlett, J. G., et al. 2009, *A&A*, 493, 753
 Bersanelli, M., Mandolesi, N., Butler, R. C., et al. 2010, *A&A*, 520, A4
 BeyondPlanck Collaboration. 2020, *A&A*, in preparation [arXiv:201x.xxxxx]
 Burigana, C., Malaspina, M., Mandolesi, N., et al. 1997, *Int. Rep. TeSRE/CNR*, 198/1997, November [arXiv:astro-ph/9906360]
 Delabrouille, J. 1998, *A&AS*, 127, 555
 Eriksen, H. K., Jewell, J. B., Dickinson, C., et al. 2008, *ApJ*, 676, 10
 Górski, K. M., Hivon, E., Banday, A. J., et al. 2005, *ApJ*, 622, 759
 Ihle et al. 2020, *A&A*, in preparation [arXiv:201x.xxxxx]
 Keihänen, E., Keskitalo, R., Kurki-Suonio, H., Poutanen, T., & Sirviö, A. 2010, *A&A*, 510, A57
 Keihänen, E., Kurki-Suonio, H., & Poutanen, T. 2005, *MNRAS*, 360, 390
 Keihänen, E., Kurki-Suonio, H., Poutanen, T., Maino, D., & Burigana, C. 2004, *A&A*, 428, 287
 Kurki-Suonio, H., Keihänen, E., Keskitalo, R., et al. 2009, *A&A*, 506, 1511
 Maino, D., Burigana, C., Górski, K. M., Mandolesi, N., & Bersanelli, M. 2002, *A&A*, 387, 356
 Maino, D., Burigana, C., Maltoni, M., et al. 1999, *A&AS*, 140, 383
 Planck Collaboration II. 2014, *A&A*, 571, A2
 Planck Collaboration II. 2016, *A&A*, 594, A2
 Planck Collaboration IV. 2016, *A&A*, 594, A4
 Planck Collaboration IV. 2020, *A&A*, 641, A4
 Planck Collaboration V. 2020, *A&A*, 641, A5
 Poutanen, T., de Gasperis, G., Hivon, E., et al. 2006, *A&A*, 449, 1311
 Prézeau, G. & Reinecke, M. 2010, *ApJS*, 190, 267
 Reinecke, M., Dolag, K., Hell, R., Bartelmann, M., & Enßlin, T. A. 2006, *A&A*, 445, 373
 Sutton, D., Johnson, B. R., Brown, M. L., et al. 2009, *MNRAS*, 393, 894
 Suur-Uski et al. 2020, *A&A*, in preparation [arXiv:201x.xxxxx]
 Wehus, I. K., Naess, S. K., & Eriksen, H. K. 2012, *ApJS*, 199, 15